

Predictive Chemical Kinetic Modeling of Pt-Catalyzed Dry Methane Reforming

Esther Ritov[†] and Alon Grinberg Dana^{*,†,‡,¶}

[†]*Wolfson Department of Chemical Engineering, Technion – Israel Institute of Technology,
Haifa 3200003, Israel*

[‡]*Grand Technion Energy Program (GTEP), Technion – Israel Institute of Technology,
Haifa 3200003, Israel*

[¶]*Resnick Sustainability Center of Catalysis, Technion – Israel Institute of Technology,
Haifa 3200003, Israel*

E-mail: alon@technion.ac.il

Phone: +972-73-378-2117

Abstract

Dry reforming of methane (DRM) over platinum catalysts offers a promising route for CO₂ utilization and syngas (H₂/CO) production, a versatile feedstock for synthetic fuels. This study employs automated chemical kinetic model generation to present a detailed microkinetic mechanism to investigate Pt-catalyzed DRM between 700-1100 K, identifying key reaction pathways and kinetic limitations through sensitivity analysis. Model predictions of CH₄ and CO₂ conversion and syngas production closely match fixed-bed experimental data across the entire temperature range and varied feed ratios. Our predictive reaction network reveals that OCX serves as a critical bottleneck intermediate for cooperative CH₄ and CO₂ activation. While CO desorption ($\text{OCX} \rightleftharpoons \text{CO} + \text{X}$) was identified as the most influential step with a strong negative sensitivity coefficient toward methane concentration, OCX regeneration ($\text{CO}_2\text{X} + \text{CX} \rightleftharpoons 2 \text{OCX}$) inhibits methane conversion by maintaining surface saturation. Methane activation follows sequential C–H scissions ($\text{CH}_4\text{X} \longrightarrow \text{CH}_3\text{X} \longrightarrow \text{CH}_2\text{X} \longrightarrow \text{CHX} \longrightarrow \text{CX}$), while CO₂ activation proceeds predominantly via a hydrogen-mediated carboxyl route ($\text{CO}_2\text{X} + \text{HX} \longrightarrow \text{COOHX} \longrightarrow \text{COX} + \text{OHX}$). Three operational regimes were identified: low-temperature desorption-limited kinetics (OCX saturation, 700-850 K), transitional pathway activation (site liberation, 850-950 K), and high-temperature distributed control with carbon management challenges (950-1300 K). These insights provide design principles for platinum-based DRM catalysts, emphasizing the importance of promoting beneficial reactions while suppressing kinetic traps and implementing temperature-specific optimization strategies to balance conversion efficiency with catalyst stability. To our knowledge, this is the first study to apply fully automated, rule-based microkinetic model generation and experimental validation to Pt-catalyzed DRM, integrating kinetic sensitivity, flux analysis, and surface speciation for catalyst design.

1. Introduction

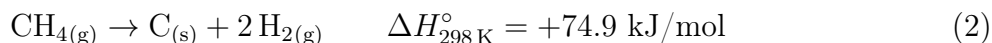
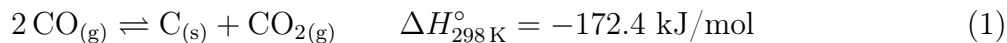
The escalating global climate crisis has placed greenhouse gas (GHG) emissions at the forefront of environmental concerns, with emissions over the last decade reaching unprecedented levels in human history.¹ One of the promising and extensively studied approaches to reduce net GHG emissions is dry reforming. This catalytic process converts carbon dioxide (CO_2) and methane (CH_4), into synthesis gas (syngas), a mixture of hydrogen (H_2) and carbon monoxide (CO).² Syngas serves as a crucial feedstock for the production of carbon-based synthetic fuels such as sustainable aviation fuel (SAF), synthetic diesel, or oxygenated hydrocarbons (e.g., methanol, dimethyl ether, and oxo-synthesis products).³

The underlying dry reforming of methane (DRM) mechanism involves four principal steps: (i) dissociative adsorption of methane, occurring preferentially at step-edge sites with CH_x fragments adopting site-specific binding geometries⁴; (ii) dissociative adsorption of CO_2 that proceeds rapidly and is strongly influenced by the surface structure and defect sites⁵; (iii) hydrogen migration from the metal to the support, leading to hydroxyl formation, particularly below 800 °C, that is associated with a fast water-gas shift reaction⁶; (iv) oxidation and desorption of intermediates such as CH_x , resulting in CO formation either directly or via carbonate-mediated reduction pathways⁷.

Despite extensive investigations, the precise surface reaction pathways remain a subject of debate, largely influenced by the catalyst structure and operating conditions. Meanwhile, practical implementation of DRM continues to encounter significant challenges.⁸ It is a highly endothermic process that requires relatively high temperatures (800-1000°C) to overcome the stability of the reactant, i.e., the high dissociation energies of CH_4 and CO_2 .⁹ While catalysts play a critical role in reducing activation energies, maintaining efficiency under these extreme conditions remains challenging.¹⁰ Several undesirable side reactions occur during the DRM process, further complicating its feasibility.¹¹ Two significant side reactions that contribute to catalyst deactivation are CH_4 cracking and the Boudouard reaction.¹² These reactions lead to the accumulation of carbon on the catalyst, significantly reducing reaction rates and

accelerating deactivation.⁶¹

The Boudouard reaction (1) predominates at lower temperatures (250-350 °C), while methane cracking (2) becomes significant at higher temperatures (600-800 °C).¹³



The Boudouard reaction is a non-elementary process that proceeds via a three-step surface mechanism involving intermediate species.¹⁴ First, CO₂ dissociatively adsorbs on a carbon-free active site, forming a surface-bound carbon–oxygen complex and releasing CO. In the second step, the surface oxygen species reacts with adsorbed carbon to produce another CO molecule, regenerating the active site. The third step describes the reverse process, in which CO re-adsorbs and reacts with surface oxygen to reform CO₂. Likewise, methane cracking is also non-elementary and proceeds through dissociative adsorption on metal surfaces.¹⁵ The mechanism involves a sequence of surface-mediated dehydrogenation steps, where methane is incrementally stripped of hydrogen atoms, ultimately leading to the deposition of elemental carbon.

These reactions increase the likelihood of coke formation, ultimately reducing the longevity and efficiency of the catalyst.^{16,17} Therefore, catalyst development is essential to improve DRM performance. The primary challenge is designing economically viable catalysts while demonstrating high activity, superior selectivity, and strong resistance to deactivation.¹⁸

Catalysts used for DRM can be classified into earth-abundant transition metals and noble metals.¹⁹ Among the transition metals, nickel (Ni) is widely studied due to its cost-effectiveness and high activity. However, Ni-based catalysts are prone to coking because they readily promote the carbon-forming side reactions mentioned above.²⁰ In contrast, noble metals, particularly platinum (Pt), exhibit superior stability under oxidative conditions,

significantly reducing carbon formation.²¹ Although noble metals offer significantly better deactivation resistance than transition metals, their high cost remains a drawback.

A deeper understanding of the elementary steps that govern the activation and conversion of a CO₂ and CH₄ mixture is essential to optimize the catalyst design and reaction conditions.⁸ Developing predictive chemical kinetic models²² that are based on fundamental reaction steps and justifiable parameters can provide valuable insights into material performance and process efficiency.^{2,9} Such advancements will establish a pivotal framework for designing catalysts that minimize deactivation caused by sintering and coking at the high temperatures (>800°C) required for substantial methane and carbon dioxide conversion during DRM,^{23,24} while enhancing our understanding of reaction pathways across temperature ranges to optimize catalytic activity.^{25,26}

This study employs predictive chemical kinetic modeling to investigate Pt-catalyzed DRM between 500-850°C. The present work aims to identify key reaction pathways and catalyst poisoning species, providing insights into temperature-dependent carbon formation and informing strategies for improved catalyst design.

2. Methods

The chemical kinetic model was generated using the Reaction Mechanism Generator (RMG) software version 3.2.0.²⁷⁻²⁹ RMG automatically explores possible intermediate species and elementary reactions for a given reacting mixture and thermodynamic conditions and utilizes a flux-based algorithm that considers the net production rates of species. The procedures implemented by RMG to iteratively expand the kinetic mechanism are extensively discussed elsewhere.^{22,27,28,30,31} Briefly, RMG automatically explores possible intermediate species and elementary reactions for a given reacting mixture using template-based rules and pre-compiled libraries. Given the initial temperature, pressure, and reactant composition, together with surface binding energies and site density, the software estimates all unknown

reaction rate coefficients and species thermodynamic properties using rate rules²⁸ and the group additivity method.³² The user sets the model expansion tolerance, which serves as the 'importance' criterion for species inclusion in the model by the flux-based algorithm.

Previously, RMG successfully generated a kinetic reaction mechanism for the heterogeneous catalysis of methane dry reforming on nickel.⁶² The present mechanism was constructed using RMG's thermodynamic libraries for Pt(111) species,^{33,34} the gas-phase H₂/O₂ system,³⁵ CCSD(T)-F12 and QCISD(T) based computations,³⁶⁻³⁸ and RMG's kinetic libraries for high-temperature catalytic partial oxidation of methane over platinum.^{39,40} Simulations were performed at temperatures of 600-1300 K (330-1030°C), a pressure of 1 bar, and inlet CH₄/CO₂ mole ratio values between 0.2-1.5. A termination rate ratio of 0.01 was used and the expansion tolerance was set at 0.05.³¹

After generating the reaction mechanism with RMG, the DRM process was simulated using a catalytic reactor model in Cantera.⁴¹ A plug-flow reactor (PFR) configuration was employed, represented as a series of perfectly mixed, constant-volume, zero-dimensional reactors with negligible pressure drop along the reactor length.

Two different reactor configurations were employed to validate the model against experimental datasets. In the first configuration, matching the Gustafson1991 study,⁴² the catalyst bed was assigned a surface-area-to-volume ratio of 1000 m⁻¹, corresponding to a monolith reactor whose central section was coated with catalytically active Pt. Operating conditions were established at a pressure of 1 bar, with a reactor diameter of 25.4 mm (1 inch), a reactor length of 0.1 m, and an inlet flow rate of 102 cm³ min⁻¹ at standard temperature and pressure (STP), yielding a calculated residence time of approximately 5.9 seconds. The model assumes an idealized Pt(111) surface, represented by a single site type (X), with a standard site density of 2.483×10^{-9} mol cm⁻².

The second configuration was designed to replicate the experimental conditions reported by Niu et al.,⁴³ using the same RMG libraries with the addition of argon to the species database. Minor modifications were applied to the RMG mechanism generation parameters,

including a surface-area-to-volume ratio of 1000 m^{-1} and a termination time of 2 seconds. Subsequently, the Cantera reactor configuration was adapted to align precisely with the reported experimental setup. The reactor geometry was scaled to an internal diameter of 10 mm and a length of 12.7 mm, while the catalyst surface-area-to-volume ratio was increased to 1500 m^{-1} . The total volumetric flow rate was set to 200 mL min^{-1} , with an inlet composition of 15% CH_4 , 15% CO_2 , and 70% Ar by volume, maintaining a 1:1 stoichiometric ratio between CH_4 and CO_2 . The gas hourly space velocity (GHSV) was calculated as $180\,000 \text{ mL}_{\text{CH}_4}/\text{h}/\text{g}_{\text{cat}}$, based on the methane flow rate and a catalyst mass of 10 mg. Temperature-dependent simulations were performed across the experimental temperature range of 450-800 °C (723-1073 K), with the reactor discretized into 7001 segments to ensure sufficient spatial resolution.

No adjustments were made to the kinetic or thermodynamic model parameters. The model presented and discussed here is purely predictive.²²

3. Results and Discussion

3.1. Benchmarking the model

The influence of temperature and feed composition on the DRM process was experimentally studied by Gustafson and Walden⁴² using a fixed-bed reactor. Our model predictions, benchmarked against their data, are presented in Figures 1 and 2, highlighting the effects of temperature and reactant feed ratios, respectively.

Figure 1 illustrates the temperature dependence of species mole fractions over the 700-1123 K range. The model successfully reproduces the experimentally observed trends for CH_4 , CO_2 , CO , and H_2 . It predicts the onset of the DRM reaction at around 800 K, and aligns reasonably well with the experimental observation. Throughout the entire temperature range, the model maintains an approximate equimolar ratio of CO to H_2 , with a slightly higher concentration of CO , as expected from the 0.9 CO_2/CH_4 feed ratio. While a minor

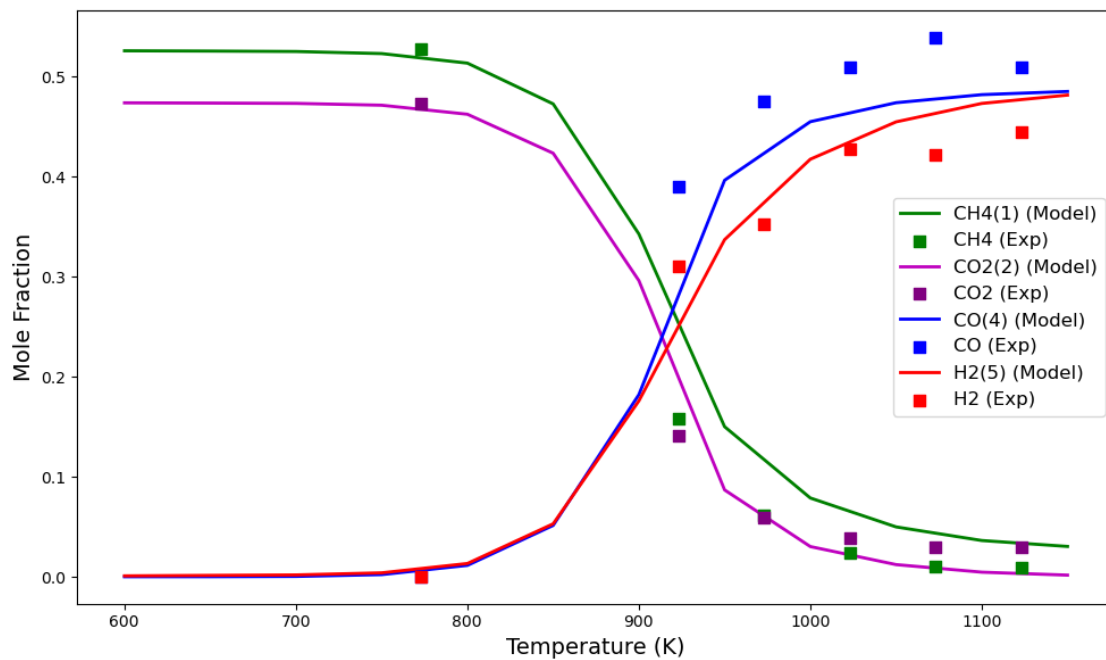


Figure 1: Comparison between experimental data (symbols)⁴² and model predictions (solid lines, this work) for Pt-catalyzed DRM with a CO_2/CH_4 feed ratio of 0.9. The upper panel presents mole fractions of CH_4 , CO_2 , CO , and H_2 as a function of temperature. The lower panel shows conversion percentages of CH_4 and CO_2 over the 700-1123 K range (500-850° C), with a residence time of 5.9 s.

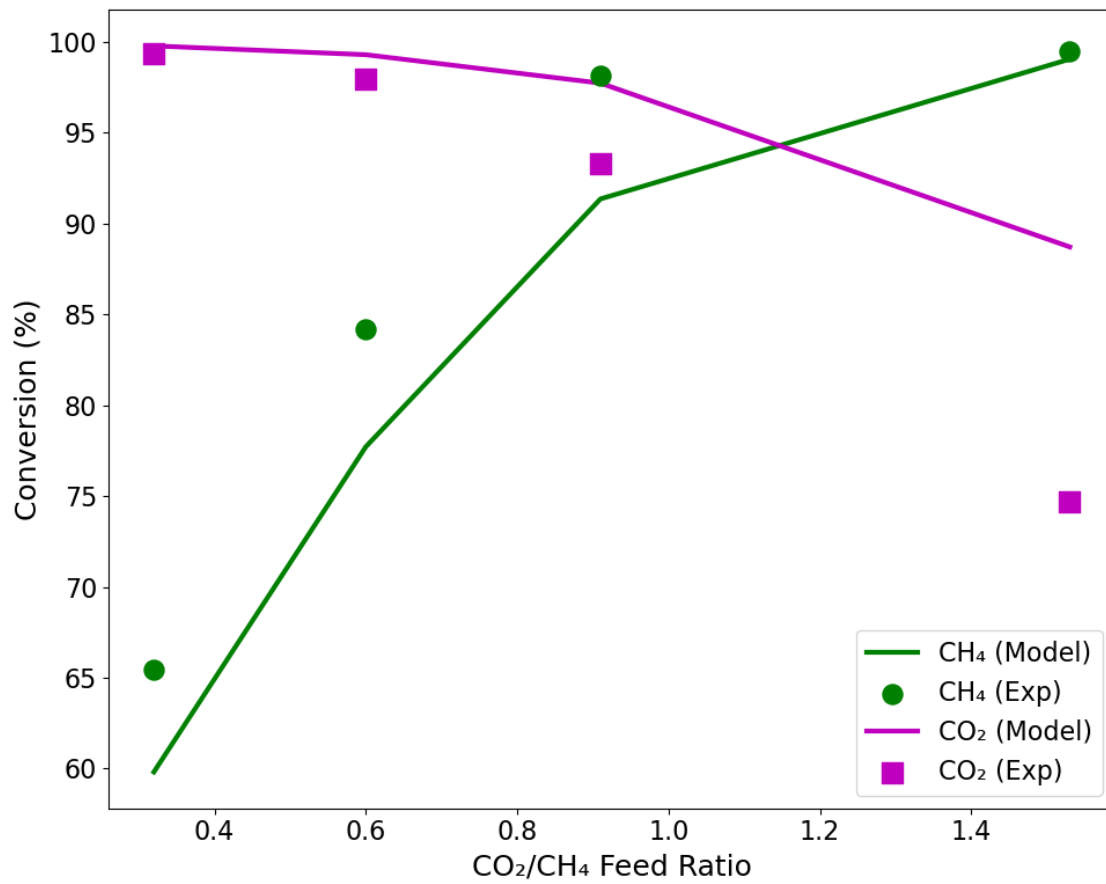


Figure 2: Conversions of CH₄ and CO₂ as a function of the CO₂/CH₄ feed ratio at 1123 K, with a residence time of 5.9 s.

over-prediction of unconverted CH_4 is observed at higher temperatures relative to CO_2 , the overall conversion trends are captured satisfactorily well by the model.

Figure 2 compares the modeled and experimental reactant conversions at 1123 K as a function of the CO_2/CH_4 feed ratio. The model captures the observed profiles reasonably well, including the decline in methane conversion and the corresponding increase in syngas production with increasing feed ratio. The model slightly over-predicts the conversion of CO_2 at the high CO_2/CH_4 feed ratio. Each reactant achieves its maximum conversion at a feed ratio corresponding to a reduced concentration of that reactant in the mixture. Across all ratios, the conversion of the limiting reactant consistently exceeds that of the excess reactant.

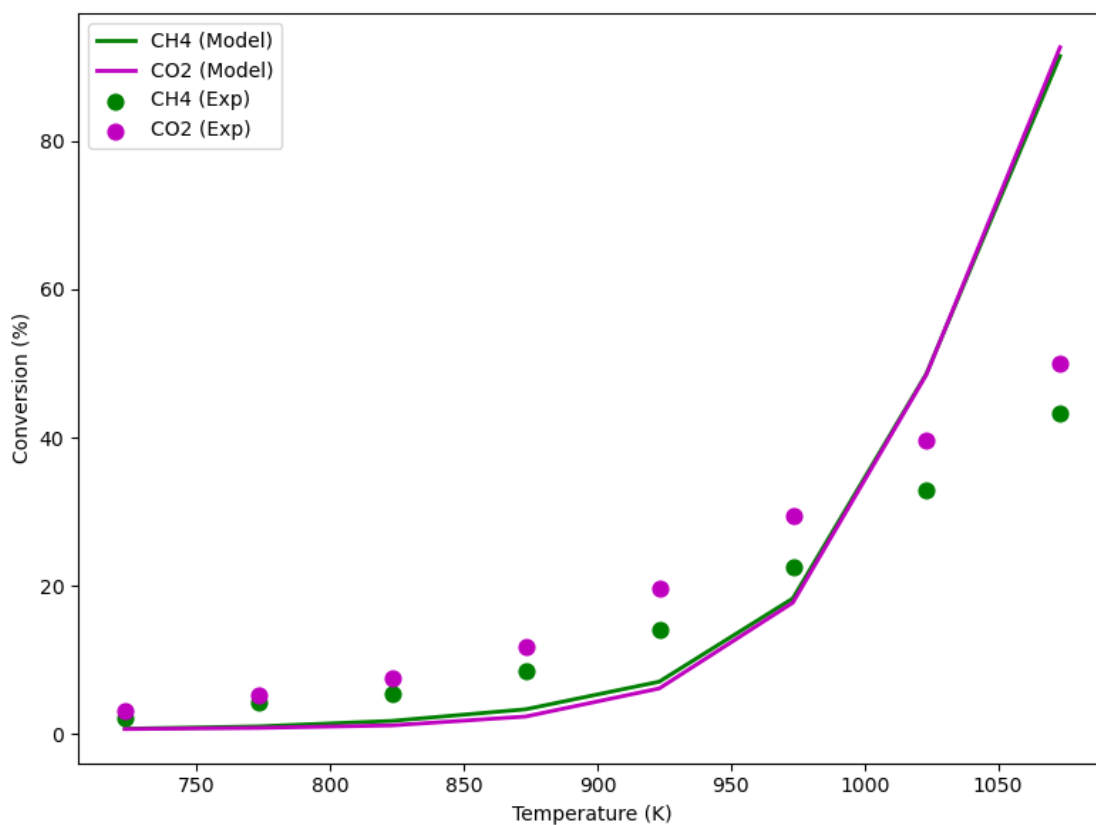


Figure 3: Comparison between experimental data (symbols)⁴³ and model predictions (solid lines, this work) for Pt-catalyzed dry reforming of methane (DRM) under a $\text{CH}_4/\text{CO}_2/\text{Ar}$ feed ratio of 0.15/0.15/0.70 at 1 bar. The plot shows conversion percentages of CH_4 and CO_2 as a function of temperature in the range of 700-1100 K, with a residence time of 0.3 s.

Figure 3 presents validation against an independent dataset under different conditions, including a shorter residence time (0.3 s), equimolar feed ratio, and dilute operation with argon. The model maintains a consistent predictive trend; however, at high temperatures, it overpredicts the conversion of both CH₄ and CO₂ compared to the experimental data. This validation, combined with the Gustafson and Walden benchmarking, demonstrates the mechanism’s robustness across diverse operating conditions and confirms its reliability for industrial applications and catalyst design.

3.2. Flux analysis

Figure 4 illustrates the detailed reaction network for the DRM process over a platinum catalyst at 1000 K. The diagram reveals an interconnected pathway architecture governed by surface adsorption and molecular activation, highlighting the major pathways responsible for hydrogen evolution and intermediate coupling.

The reaction network predominantly follows C₁-based pathways, in line with the mechanistic framework established for platinum-catalyzed methane activation.^{44,45,63} Methane activation proceeds via a stepwise C–H bond scission sequence on platinum surface sites, captured in the dehydrogenation progression:



Among these, the dissociation of CHX to CX and HX ($\text{CHX} \rightleftharpoons \text{CX} + \text{HX}$) is frequently identified as a kinetically significant barrier, based on both kinetic modeling and Density Functional Theory (DFT) studies.⁴⁶ This fourth C–H cleavage is often considered rate-limiting in methane activation on transition metals due to the high activation energy required to rupture the final C–H bond on the surface.

Its central position in the flux diagram-bridging the CH_x intermediates with surface-bound carbon formation-highlights its role as a mechanistic junction between upstream dehy-

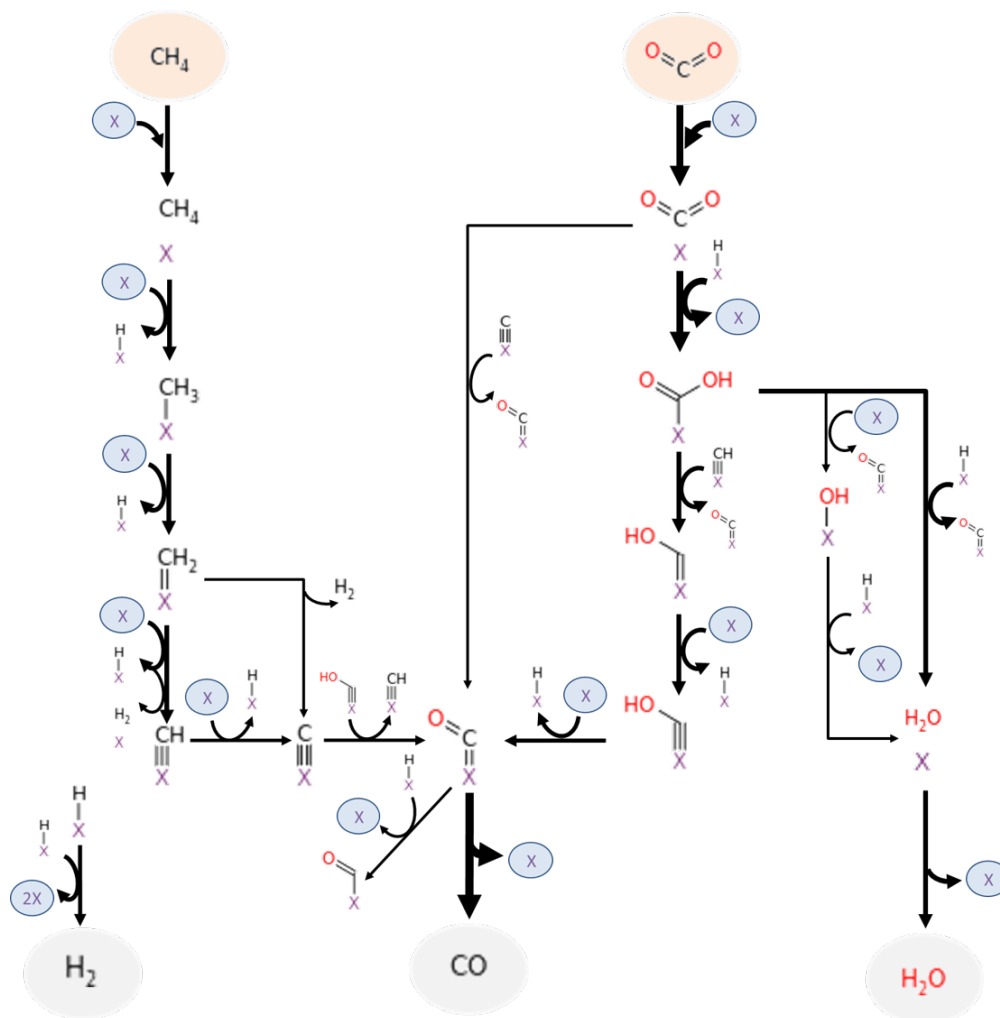
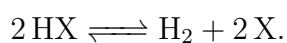


Figure 4: Detailed reaction network for the DRM process over a platinum catalyst. CO_2/CH_4 feed ratio=0.9, $\tau = 5.9$ s

drogenation and downstream oxidation pathways. Each dehydrogenation step concurrently generates adsorbed hydrogen atoms (HX), which desorb via recombination:



This step constitutes the primary pathway for molecular hydrogen formation, visible in the left region of the reaction network, and is essential for maintaining active site availability and sustaining the reforming cycle.

On the CO_2 side, activation predominantly follows a hydrogen-assisted pathway: $\text{CO}_2\text{X} +$

$\text{HX} \rightleftharpoons \text{COOHX}$. This route exhibits a significantly lower activation barrier (72.0 kJ/mol) compared to direct CO_2 dissociation (174.5 kJ/mol),⁴⁶ underscoring the thermodynamic and kinetic favorability of the COOHX intermediate. The importance of this pathway is also reflected in the reaction flux diagram, where the carboxyl route dominates over alternatives.

Li et al.⁴⁷ observed characteristic bands between 1000-2000 cm^{-1} corresponding to O-C-O vibrational modes on Pt/CeO₂ catalysts, which they attributed to adsorbed carboxyl (COOH), formate (HCOO), and carbonate species. Similarly, Mierczynski et al.⁴⁸ demonstrated through FTIR spectroscopy that CO₂ on Ni/CeO₂ catalysts can be hydrogenated to form COOH intermediates, which subsequently undergo further hydrogenation to bicarbonates, supporting the hydrogen-assisted CO₂ activation pathway.

Following its formation, the carboxyl intermediate undergoes C-O bond cleavage via $\text{COOHX} \rightleftharpoons \text{COX} + \text{OHX}$, facilitating the generation of CO. In contrast, the competing formate pathway (HCOOX) is more endothermic and associated with higher energy barriers, making it kinetically less favorable and thus less significant in the overall mechanism.

The carboxyl intermediate plays a central role, facilitating C-O bond scission to yield CO ($\text{COOHX} \rightleftharpoons \text{COX} + \text{OHX}$). In contrast, the formate pathway (HCOOX, not shown) involves higher barriers and is more endothermic, making it kinetically less favorable. Since HX species are a major product of hydrocarbon dehydrogenation, the hydrogen-mediated CO₂ activation pathway serves as a key coupling junction between the CH₄ and CO₂ sub-networks. This synergy is further enhanced by hydrogen spillover, where surface hydrogen generated from CH₄ dehydrogenation migrates across the surface to promote CO₂ activation. The phenomenon of hydrogen spillover on platinum-containing catalysts is well-established,⁵⁶⁻⁵⁸ and its role in facilitating DRM-relevant processes has been directly demonstrated.⁵⁹

A key mechanistic feature revealed in the network is the direct reaction between surface carbon species and adsorbed carbon dioxide, $\text{CX} + \text{CO}_2\text{X} \rightleftharpoons 2\text{COX}$, which serves as another crucial coupling junction between the degradation pathways of the two primary reactants. This Langmuir-Hinshelwood mechanism⁴⁹ proceeds via the reaction of two surface-

bound species, CX and CO₂X, and enables the conversion of inert carbon deposits into mobile COX species, playing a dual role in both CO formation and catalyst reactivation.

The central region of the flux diagram captures the sequential oxidation pathways of adsorbed methylidyne species (CHX). Our analysis indicates that the oxidation of CHX predominantly proceeds via COOH-mediated oxygen transfer, as exemplified by the elementary step $\text{CHX} + \text{COOHX} \longrightarrow \text{CH}_2\text{OX} + \text{OCX}$. This pathway, involving the reaction between an adsorbed CHX and an adsorbed carboxyl intermediate (COOHX), leads to the formation of a partially oxidized carbon species (CH₂OX) and adsorbed carbon monoxide (OCX). While specific experimental verification of this exact elementary step is complex to isolate directly in DRM on platinum, numerous DFT studies on carbon oxidation and oxygen transfer mechanisms on platinum group metals provide strong theoretical support for the high reactivity of surface carboxyl species as oxygen donors, and for their preference over hydroxyl-mediated pathways for oxidizing carbonaceous species.⁵⁰⁻⁵³ This finding highlights the crucial role of oxygen-containing surface species, specifically COOHX, in oxidizing carbonaceous intermediates within the reaction network.

The preferential reactivity of carboxyl intermediates in carbon oxidation processes on platinum surfaces is well-supported by comprehensive DFT studies,⁵⁰⁻⁵² which demonstrate that COOH dehydrogenation proceeds readily on Pt(111) and that carbon oxidation products, such as CO and CO₂, are primarily formed through COOH intermediate pathways in related reactions such as formic acid decomposition. Furthermore, the significant role of COOH intermediates in the mechanism of the water-gas shift reaction on Pt catalysts has been established through first-principles calculations and microkinetic modeling.⁵⁴ Microkinetic modeling efforts for methane reforming and related reactions on platinum-group metals have also emphasized the importance of various intermediates in their proposed reaction mechanisms.⁵⁵

The interconnected nature of these pathways underscores how platinum catalysts achieve high DRM performance through coordinated activation of both reactants. Collectively, the

reaction network reveals critical trade-offs between activity and selectivity. Computational validation supports the flux preferences and intermediate distributions shown. The centrality of COOH intermediates, the role of hydrogen spillover and hydrogen-assisted mechanisms, and the kinetic accessibility of key elementary steps emerge as defining factors that govern DRM performance over Pt catalysts.

3.3. Kinetic Sensitivity Analysis

The kinetic sensitivity analysis of DRM over a platinum catalyst, performed at 900 K and 1000 K with a CO₂/CH₄ feed ratio of 0.9 and a residence time of 5.9 seconds, illustrates temperature-dependent reaction dynamics and pinpoints the critical pathways governing methane conversion. These two temperatures represent about 70% and 20% conversion of CH₄, respectively (Figure 1). The normalized sensitivity coefficients, shown in Figure 5, quantify the effect of perturbations in individual rate coefficients on methane concentration, providing insights into the controlling reaction pathways and how their influence shifts with temperature. By examining normalized sensitivity coefficients, we gain quantitative insights into how key individual elementary surface reactions influence the overall process, focusing here (Figure 5) on the concentration of methane as the observable.

Figure 6 presents the normalized sensitivity coefficients for methane conversion with respect to the catalyst’s surface area to volume ratio (S/V), plotted on a logarithmic scale as a function of temperature. This metric quantifies the direct impact of catalyst surface availability on the overall reaction efficiency. The resulting curve reveals a strongly temperature-dependent regime characterized by three distinct behaviors.

Below approximately 950 K, the sensitivity remains high and nearly constant, maintaining values close to 1. This indicates that the conversion is critically limited by the available catalytic surface area, consistent with the trends seen in total site coverage (Figure 7). In this regime, the catalyst surface is predominantly saturated with adsorbed intermediates such as CHX, OCX, and HX (Figure 8). These strongly-bound species limit the number of

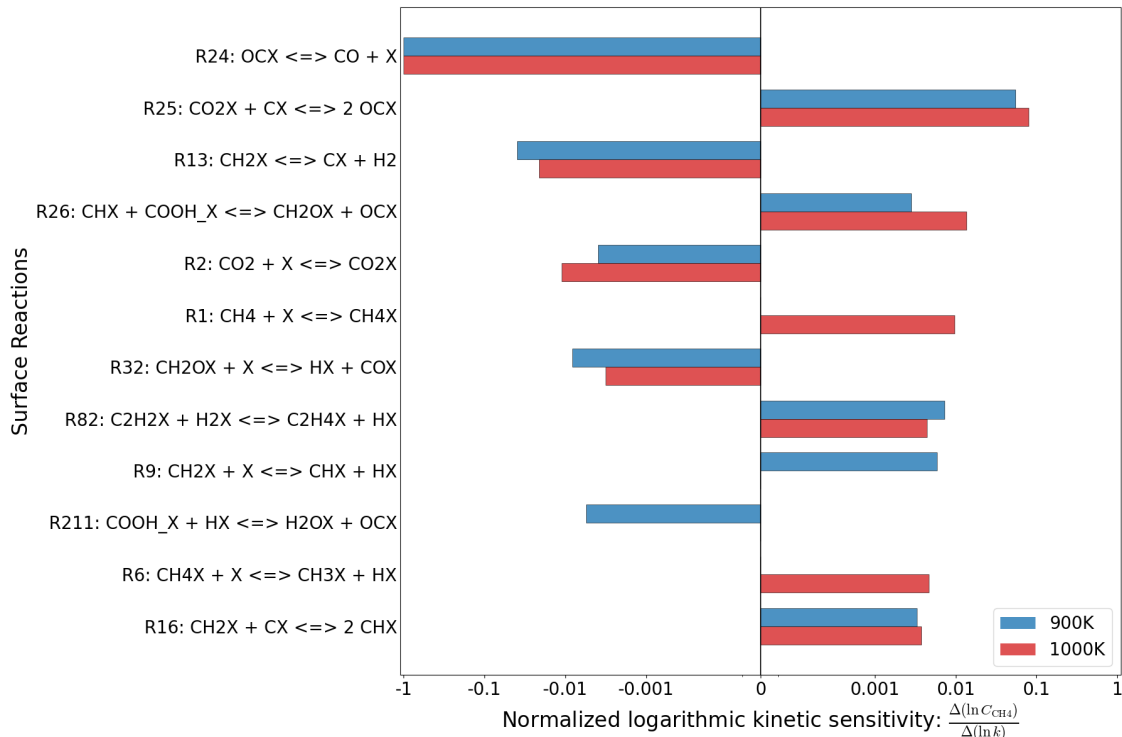


Figure 5: Normalized kinetic sensitivity coefficients, shown on a logarithmic scale, for the concentration of CH_4 in DRM over a platinum catalyst at 900 K and 1000 K, highlighting the temperature-dependent shift in rate-determining steps. Negative sensitivity coefficients indicate reactions that promote methane consumption when the respective rate coefficient slightly increases, and vice versa.

free active sites, and thus increasing the surface area directly alleviates the kinetic bottleneck, resulting in enhanced conversion.

Between approximately 950 K and 1000 K, the sensitivity exhibits a sharp and abrupt decline, spanning over four orders of magnitude (from $\sim 10^0$ to $\sim 10^{-4}$). This dramatic transition reflects a major reorganization in surface kinetics, driven by an increase in temperature that facilitates desorption and site liberation. As a result, the system's dependence on the macroscopic S/V ratio diminishes rapidly. This indicates a shift in the rate-limiting step from site-limited adsorption/reaction to regimes potentially dominated by gas-phase mass transfer or intrinsic surface kinetics, where turnover frequencies are no longer constrained by surface availability.

Above approximately 1000 K, the sensitivity gradually increases again, although it re-

mains very low ($\sim 10^{-4}$ to $\sim 10^{-3}$). This subtle rise suggests a weak re-emergence of S/V dependency. At these elevated temperatures, rapid desorption kinetics allow for fast regeneration of surface sites. Thus, even small increases in surface area can still improve conversion marginally by increasing the density of these rapidly cycling sites. This effect could also be linked to the activation of new, more demanding high-temperature pathways requiring specific surface interactions.

Further support for these interpretations comes from the kinetic sensitivity analysis (Figure 5), which highlights the changing role of key elementary steps. Notably, $\text{OCX} \rightleftharpoons \text{CO} + \text{X}$ (R24) and recombination reactions (e.g., R211) become increasingly relevant with temperature, influencing CH_4 conversion and contributing to the observed regime transitions.

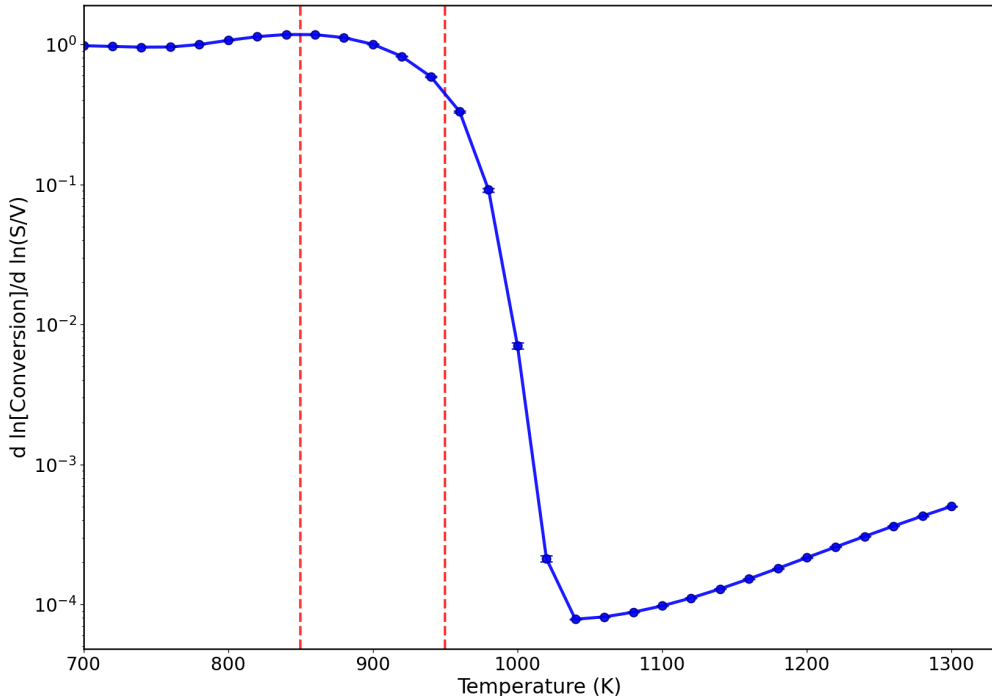


Figure 6: Temperature dependence of methane conversion sensitivity to variations in the surface area to volume ratio (S/V). The normalized sensitivity coefficient $\frac{d \ln[\text{Conversion}]}{d \ln(S/V)}$ was computed by perturbing the S/V ratio by +5% around a baseline value of 1000 m^{-1} . The y-axis is shown on a logarithmic scale. Vertical dashed lines indicate key transition boundaries near 850 K and 950 K.

Reaction R24, $\text{OCX} \rightleftharpoons \text{CO}_{(g)} + \text{X}$, exhibits the highest absolute normalized sensitivity coefficient value, displaying a strong negative sensitivity at both temperatures, indicating

that increasing the CO desorption rate coefficient has the strongest effect on promoting CH₄ consumption. The OCX species serves as a critical rate determining step in the reaction network (Figure 4), serving as a key intermediate that connects multiple competing pathways. The extreme negative sensitivity coefficient of R24 (an order of magnitude larger than all other sensitivity coefficients in absolute terms) reveals that CO desorption from surface-bound OCX represents the primary kinetic bottleneck in the catalytic cycle. When this desorption step is accelerated, it rapidly clears OCX intermediates from the surface, freeing active sites and driving the overall reaction network forward.

This depletion effect is balanced by the compensating reaction R25, $\text{CO}_2\text{X} + \text{CX} \rightleftharpoons 2\text{OCX}$, which shows strong positive sensitivity at both temperatures. R25 regenerates OCX by consuming both CO₂X and surface carbon (CX). Its positive sensitivity indicates that accelerating this regeneration pathway actually inhibits the overall methane conversion. The sensitivity analysis thus reveals a delicate optimization balance: sufficient CO desorption (R24) must occur to prevent kinetic bottlenecks, but excessive OCX regeneration (R25) can destabilize the catalytic cycle.

The dehydrogenation step R13, $\text{CH}_2\text{X} \rightleftharpoons \text{CX} + \text{H}_2$ displays strong negative sensitivity toward CH₄ concentration, indicating its critical role in promoting methane conversion at both examined temperatures. In the flux network (Figure 4), both CH₂X and CX are major intermediates, and the negative sensitivity coefficient of R13 suggests that enhancing its rate accelerates the overall reaction flux by efficiently converting methane-derived carbon species to valuable hydrogen product. This reaction serves a dual role: it produces CX, which can serve as a carbon reservoir, and H₂, a desired product. The network interpretation reveals that R13 acts as a carbon flux regulator that maintains the balance between carbon utilization and hydrogen production. Its consistently negative sensitivity coefficient at both temperatures identifies R13 as a pivotal control point for both performance optimization and carbon management in the catalytic system.

Reactions R2, $\text{CO}_2 + \text{X} \rightleftharpoons \text{CO}_2\text{X}$, and R32, $\text{CH}_2\text{OX} + \text{X} \rightleftharpoons \text{HX} + \text{OCX}$, exhibit

negative sensitivity coefficients at both temperatures, indicating that they consistently promote methane conversion across the operating range. R2 represents CO₂ adsorption that facilitates the overall conversion process, contrary to intuitive expectations of site competition. The negative sensitivity of R2 at both temperatures suggests that CO₂ adsorption creates favorable surface conditions or provides essential CO₂X intermediates that enhance the reforming efficiency. R32 involves the transformation of CH₂OX intermediates, generating surface hydrogen (HX) and carbonyl species (OCX). Its negative sensitivity coefficient at both temperatures indicates that accelerating this transformation promotes methane conversion by facilitating intermediate processing and maintaining optimal surface speciation.

Four reactions exhibit temperature-dependent sensitivity patterns that reveal the evolving kinetic landscape. Reactions R82, $C_2H_2X + H_2X \rightleftharpoons C_2H_4X + HX$, R9, $CH_2X + X \rightleftharpoons CHX + HX$, and R211, $COOH_X + HX \rightleftharpoons H_2OX + OCX$, show negative sensitivity primarily at 900 K, indicating that they promote methane conversion under lower-temperature conditions. These reactions represent alternative pathways that become kinetically relevant when the main reaction network operates at moderate activity levels.

R9 provides an alternative CH₂X transformation route that competes with the dominant R13 pathway, while R82 involves C–C coupling reactions that may contribute to carbon utilization. R211 represents a hydrogen-assisted intermediate coupling that generates water and regenerates OCX. At 1000 K, these alternative pathways become kinetically overshadowed by the dominant routes, demonstrating temperature-dependent pathway activation. These four reactions display clear differences in their sensitivity coefficients between the two temperatures (900K vs 1000K), either by appearing at only one temperature or showing significantly different magnitudes at the two temperatures.

The emergence of R1, $CH_4 + X \rightleftharpoons CH_4X$, exclusively at 1000 K with positive sensitivity reflects a fundamental shift in methane activation behavior and represents the fourth temperature-dependent reaction. At 900 K, the low sensitivity of R1 indicates that conventional methane activation routes, $CH_4 \longrightarrow CH_3X \longrightarrow CH_2X \longrightarrow CHX$, are sufficient due

to favorable kinetics and adequate surface site availability. However, at 1000 K, R1 emerges with positive sensitivity, suggesting that this major pathway begins to compete with or interfere with more efficient routes. The positive sensitivity indicates that while R1 provides an additional methane activation mechanism, its enhancement inhibits overall conversion, possibly due to formation of less reactive CH_4X species that act as kinetic dead-ends or occupy surface sites unproductively.

Additional temperature-dependent reactions emerge at 1000 K with distinct sensitivity patterns. Reaction R6, $\text{CH}_4\text{X} + \text{X} \rightleftharpoons \text{CH}_3\text{X} + \text{HX}$, has a positive sensitivity coefficient exclusively at 1000 K, indicating that while this reaction attempts to reactivate surface carbon species by converting them to CH_3X , its acceleration actually inhibits overall methane conversion. This suggests that the CH_4X species generated by R1 create a kinetic trap, where reactivation through R6 diverts surface sites and intermediates from more efficient pathways. R16: $\text{CH}_2\text{X} + \text{CX} \rightleftharpoons 2\text{CHX}$ appears at both temperatures but shows enhanced (more negative) sensitivity at 1000 K, indicating it promotes methane conversion by efficiently recycling both methane-derived CH_2X and accumulated CX into reactive CHX intermediates. This reaction effectively doubles the availability of active carbon species, underscoring the importance of carbon recycling mechanisms at elevated temperatures where carbon management becomes critical for sustained catalytic performance.

3.4. Implications for Catalyst Design and Side Reactions

Figure 7 traces the evolution of total surface coverage from 700 to 1300 K and reveals three distinct regimes traced by inflection points in the second derivative. At low temperatures (700-790 K), the surface is saturated ($\sim 100\%$ coverage), predominantly by adsorbed hydrogen species (HX), as clearly demonstrated in Figure 8. In this regime, free sites for methane activation are nearly absent due to hydrogen poisoning, and hydrogen desorption processes compete with other desorption steps for kinetic control, exhibiting a strong sensitivity in the reaction network. The second derivative plot (bottom of Figure 7) quantitatively delineates

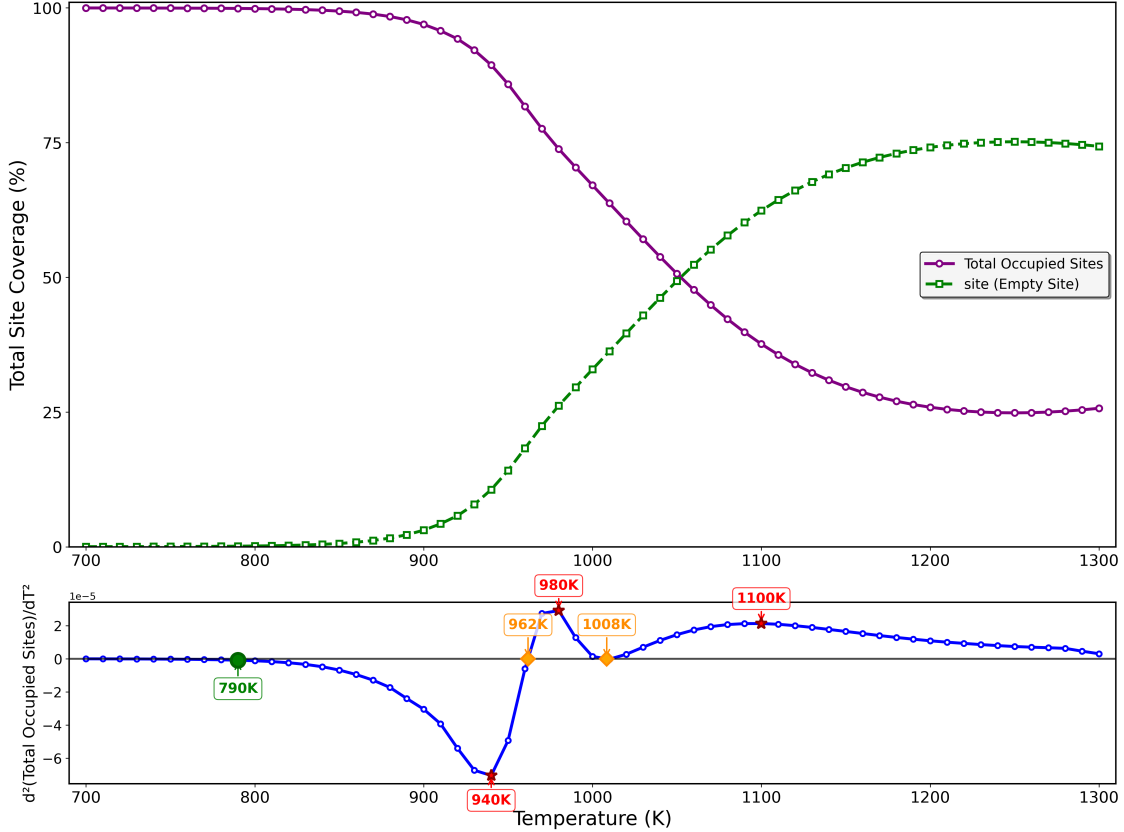


Figure 7: Temperature-dependent surface site coverage and its second derivative. Top: Total occupied sites (purple) and empty sites (green) as a function of temperature reveal three operational regimes. Bottom: Second derivative of total site coverage (blue) identifies regime transitions: (i) surface saturation regime (790-980 K), with early onset detection at 790 K marking initial deviation from hydrogen-dominated saturation; (ii) transitional regime (980-1100 K), marked by zero crossings at 962 K and 1008 K (50% site crossover); (iii) high-activity regime (1100-1300 K), where free sites dominate ($\sim 75\%$) with near-zero curvature indicating thermodynamic stability.

these regimes. The early onset detection at 790 K captures initial breakdown of hydrogen saturation. The most negative peak at 940 K in $d^2(\text{Total Occupied Sites})/dT^2$ identifies the onset of rapid surface liberation, a critical temperature where hydrogen-dominated saturation collapses. The zero crossing at 962 K marks the deceleration of cooperative desorption, while the inflection at 1008 K coincides with the 50% coverage crossover. The approach to near-zero curvature above 1100 K confirms thermodynamic stability.

Between 940 K and 1100 K, a transitional regime emerges where the surface undergoes dramatic speciation changes. The sharp desorption onset at 940 K initiates rapid HX desorp-

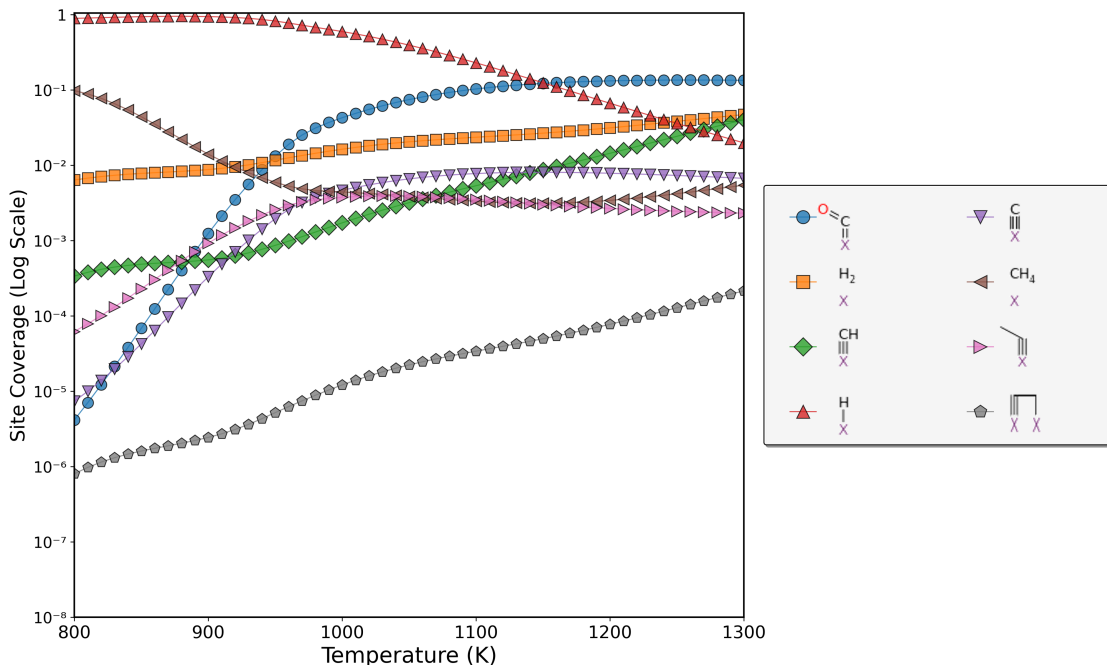


Figure 8: Species-resolved surface coverage profiles across temperature. HX (red triangles) dominates at low temperatures, OCX (blue circles) peaks in mid-range, while CHX (green diamonds) and CX (purple right-pointing triangles) buildup dominates at high temperatures, reflecting transitions between different catalytic regimes.

tion, while OCX coverage (blue circles) increases and reaches its peak around 1000-1100 K. Within this window, the total site coverage drops from $\sim 95\%$ to $\sim 25\%$, activating methane-derived pathways: coverage of CHX intermediates (green diamonds) emerges and increases substantially from $\sim 10^{-3}$ to $\sim 10^{-2}$, while H₂X species (orange squares) show sustained presence indicating active reforming. The critical crossover at 1008 K marks where occupied and empty sites reach equal coverage (50% each). Kinetic control shifts from being dominated by hydrogen management to a more distributed network involving both C-H bond cleavage and CO₂-mediated oxidation.

Above 1100 K, the surface enters a high-activity regime characterized by sustained site availability ($\sim 75\%$ empty sites). The OCX species reach their maximum and begin to plateau, while dramatic accumulation of surface carbon species occurs, most notably CX (purple right-pointing triangles) which increases exponentially from $\sim 10^{-5}$ at 950 K to $\sim 10^{-3}$ at 1300 K, signaling potential for coke nucleation. The H₂X coverage achieves

its highest levels ($\sim 10^{-1}$), indicating maximum hydrogen production capacity and strong reforming activity.

The emergence and peak of OCX in the mid-temperature range confirms that CO₂ dissociation becomes favorable as sites are liberated, with the sensitivity analysis at 1000 K revealing a dramatic redistribution of kinetic control. While CO desorption (R24) remains negatively sensitive, its magnitude decreases as site availability improves, and methane dehydrogenation steps (R13: $\text{CH}_2\text{X} \rightleftharpoons \text{CX} + \text{H}_2$, R6: $\text{CH}_4\text{X} \rightleftharpoons \text{CH}_3\text{X} + \text{HX}$) develop positive sensitivities, confirming the activation of methane conversion pathways as HX coverage declines and CHX species emerge. The appearance of positive sensitivity for reforming-related reactions indicates that C-H bond cleavage and hydrogen management become kinetically relevant, consistent with the observed emergence of H₂X and CHX species.

These trends support the multi-step Boudouard and methane cracking mechanisms described earlier. The OCX dominance (blue circles) reflects initial CO₂ dissociation steps, the emergence of CHX (green diamonds) and HX (red triangles) confirms sequential methane dehydrogenation, and CX accumulation (purple down-pointing triangles) represents the final carbon products of both pathways. The progression from an HX-dominated surface through the OCX peak to CX accumulation validates the mechanistic sequence in which hydrogen management transitions to carbon-oxygen chemistry and ultimately to carbon deposition pathways beginning around 950 K.

The exponential rise in CX coverage from 950 K aligns with coke formation observed in TGA studies,⁶⁰ though the model captures only chemisorbed species. As shown in Figure 8, CX coverage (purple right-pointing triangles) increases dramatically from $\sim 10^{-5}$ to $\sim 10^{-3}$ between 950 K and 1300 K, representing a hundred-fold increase that signals the onset of coke precursor formation. Thus, the model provides valuable predictive insight into the early stages of coke nucleation, demonstrating the progression from hydrogen poisoning through active reforming to potential carbon accumulation, with carbon-carbon coupling reactions (R16: $\text{CH}_2\text{X} + \text{CX} \rightleftharpoons 2 \text{CHX}$) showing increased sensitivity in the high-activity regime.

To optimize catalyst performance across these regimes, different strategies are required based on the sensitivity-identified rate-controlling steps. In the saturation regime (790-980 K), promoting hydrogen desorption through support modification or metal-support interactions is essential to accelerate liberation from HX dominance, while enhancing positive sensitivity reactions (R25, R1) can improve site utilization. In the transitional regime (980-1100 K), careful balance between OCX formation and CHX accumulation is needed, with precise temperature control around the critical 1008 K crossover. In the high-activity regime (above 1100 K), the exponential CX growth necessitates carbon management strategies to prevent irreversible accumulation through carbon-recycling pathways and controlling carbon-carbon coupling reactions.

The species-resolved analysis reveals that surface poisoning mechanisms vary across regimes from hydrogen poisoning at low temperatures to potential carbon poisoning at high temperatures. This highlights the value of combining surface speciation analysis with kinetic sensitivity metrics to guide catalyst design for both high performance and long-term stability across the entire operational range.

4. Conclusion

In this work, we have developed and validated a detailed predictive microkinetic model for Pt-catalyzed dry reforming of methane (DRM) over the 700-1300 K range using the Reaction Mechanism Generator (RMG) software. The model captures reasonably well the temperature-dependent specie profiles measured across 700-1150 K, validated against observed species concentrations, and analyzed using flux and kinetic sensitivity data. The suggested model also captures the temperature- and feed-ratio-dependent methane and carbon-dioxide conversions, as well as syngas product ratios, reproducing the onset of reforming near 800 K and the equimolar CO/H₂ trend at higher temperatures.

A comprehensive flux analysis at 1000 K reveals a tightly coupled network in which

methane dehydrogenation proceeds through sequential C–H scissions (ultimately yielding CX), while CO₂ activation follows a hydrogen-mediated carboxyl pathway. Surface-carbon oxidation is dominated by carboxyl transfer to CH_x species and by direct reaction of CX with CO₂X (Langmuir–Hinshelwood coupling), illustrating the pivotal role of COOH intermediates and hydrogen spillover in maintaining catalytic turnover and in preventing coke formation.

The kinetic sensitivity analysis at 900 K (~70% CH₄ conversion) and 1000 K (~90% conversion) identified the key rate-controlling steps and their temperature dependence. The CO desorption reaction ($\text{OCX} \rightleftharpoons \text{CO} + \text{X}$) is the most influential step, with extreme negative sensitivity coefficients, revealing desorption-limited kinetics under high surface coverage. Counterintuitively, OCX regeneration ($\text{CO}_2\text{X} + \text{CX} \rightleftharpoons 2\text{OCX}$) shows positive sensitivity for CH₄ concentration, indicating that excessive regeneration inhibits methane conversion by maintaining surface saturation and diverting intermediates from productive pathways. The fourth C–H scission ($\text{CH}_2\text{X} \rightleftharpoons \text{CX} + \text{H}_2$) is the most beneficial reaction for increased CH₄ conversion at all studied conditions, making it a prime target for catalyst design.

Surface coverage analysis revealed three distinct regimes: (1) desorption-limited kinetics at low temperatures (700–850 K) with near-complete site saturation, (2) pathway diversification during site liberation (850–950 K), and (3) distributed kinetic control with carbon management challenges at high temperatures (950–1300 K). In the COX-saturated regime, promoters or supports that lower the OCX desorption barrier will be most effective. In the transition regime, balancing CH_x binding strength to sustain negative sensitivity in dehydrogenation is critical. At high temperatures, catalysts must combine strong carbon-recycling activity with suppression of C₂-forming and deep-hydrogenation routes to prevent deactivation. These mechanistic insights establish design principles for platinum-based DRM catalysts that achieve both high conversion and operational stability through temperature-dependent kinetic control strategies.

The model predicts that CO* desorption initiates around 950–1000 K, and identifies an

optimal operating window between 1000–1100 K where DRM activity is maximized while carbon accumulation is minimized, providing clear, experimentally testable targets for validation, and long-term catalyst stability tests.

Overall, our results demonstrate that a network-level perspective, integrating flux analysis, sensitivity analysis, and surface speciation, can unambiguously identify the elementary steps that govern activity, selectivity, and stability in DRM. These insights provide concrete guidelines for rational design of Pt-based catalysts and reaction conditions that maximize syngas yields while mitigating coke formation under industrially relevant high-temperature conditions.

Supporting Information Available

- The RMG input file that was used to generate the model
- The RMG species dictionary
- The Chemkin format gas phase model
- The Chemkin format surface model

Acknowledgement

This research was supported in part by the Boeing-Technion SAF Innovation Center funded by the Boeing Company. Financial support from the Stephen and Nancy Grand Technion Energy Program (GTEP) is gratefully acknowledged. E.R. acknowledges funding through the Israel Scholarship Education Foundation (ISEF).

References

- (1) IPCC. *Climate Change 2022: Mitigation of Climate Change*. Working Group III Contribution to the Sixth Assessment Report, Intergovernmental Panel on Climate Change, Geneva, Switzerland, 2022.
- (2) Kongzhai Li, Chao Su, Lei Jin, Beibei He, and Qingcai Liu. Progress in catalysts for methane reforming with carbon dioxide: A review. *Energy & Fuels*, 37:9573–9596, 2023.
- (3) Feng Wang, Tao Zhang, Yang Liu, and Yongdan Li. Recent advances in plasma-assisted CO₂ reforming of methane. *Chemical Engineering Journal*, 472:145967, 2024. 10.1016/j.cej.2023.145967.
- (4) Jingguang Wei and Enrique Iglesia. Mechanism and site requirements for activation and chemical conversion of methane on supported pt clusters and turnover rate comparisons among noble metals. *The Journal of Physical Chemistry B*, 108(13):4094–4103, 2004.
- (5) Knut Wittich, Michael Krämer, Nils Bottke, and Stephan A. Schunk. Catalytic dry reforming of methane: Insights from model systems. *ChemCatChem*, 12(8):2130–2147, 2020. 10.1002/cctc.201902142.
- (6) Roel Prins. Hydrogen spillover. facts and fiction. *Chemical Reviews*, 112(5):2714–2738, 2012. 10.1021/cr200346z.
- (7) Haibin Zhu, Huichao Chen, Menghan Zhang, Cai Liang, and Lunbo Duan. Recent advances in promoting dry reforming of methane using nickel-based catalysts. *Catalysis Science & Technology*, 14:1712–1729, 2024. 10.1039/D3CY01612A.
- (8) Ningbo Gao, Guangjie Han, Hongyu Tian, and Aijuan Wang. Advanced catalyst design strategies for dry reforming of methane. *Materials Today Sustainability*, 24:100295, 2023.

- (9) Xiaobo Chen, Baojuan Dou, Chunyu Wang, Yuqing Song, Hongmei Zhang, Chunmei Xu, and Wei Wang. Design strategies and performance enhancement of perovskite-based catalysts for dry reforming of methane. *Renewable and Sustainable Energy Reviews*, 182:113431, 2023.
- (10) Wenwen Zheng, Jian Zhang, Chao Xie, Yanyan Zhang, and Hongyang Liu. Recent advances in nickel-based catalysts for dry reforming of methane. *Energy & Environmental Science*, 16:1841–1869, 2023.
- (11) Ali Hamzehee Pour, Ali Asghar Mirzaei, Ahmad Tofigh, and Shohreh Fatemi. Recent progress in dry reforming of methane: A review of catalytic performance, deactivation mechanisms, and future prospects. *Chemical Engineering Journal*, 464:142711, 2023. 10.1016/j.cej.2023.142711.
- (12) Manish Kumar, Amit Awasthi, and Anil Suresh Kumar Sinha. Recent advances in catalyst development for dry reforming of methane: A review. *Renewable and Sustainable Energy Reviews*, 181:113178, 2023. 10.1016/j.rser.2023.113178.
- (13) National Institute of Standards and Technology. *NIST Chemistry WebBook*. NIST Standard Reference Database Number 69, 2025. URL <https://webbook.nist.gov/chemistry/>.
- (14) Colomba Di Blasi. Combustion and gasification rates of lignocellulosic chars. *Progress in Energy and Combustion Science*, 35(2):121–140, 2009. 10.1016/j.pecs.2008.08.001.
- (15) Sirui Tong, Bin Miao, Lan Zhang, and Siew Hwa Chan. Decarbonizing natural gas: A review of catalytic decomposition and carbon formation mechanisms. *Energies*, 15(7), 2022. 10.3390/en15072573.
- (16) Bawadi Abdullah, N Arun Kumar, M F Husin, and S K Kamarudin. A critical review of dry reforming of methane over ni-based catalysts. *International Journal of Hydrogen Energy*, 47(83):35825–35849, 2022. 10.1016/j.ijhydene.2022.08.184.

- (17) Rui-Qin Zhang, Guo-Dong Li, and Xiao-Xiong Zou. Recent advances in catalysts for efficient dry reforming of methane. *Energy & Environmental Materials*, 5(1):20–42, 2022. 10.1002/eem2.12291.
- (18) Nadia Aoun Khalil Aramouni, Jimmy George Touma, Bassam Abu Tarboush, Joseph Zeaiter, and Mohammad Naji Ahmad. Catalyst design for dry reforming of methane: Analysis review. *Renewable and Sustainable Energy Reviews*, 82:2570–2585, 2018. 10.1016/j.rser.2017.09.076.
- (19) Abdul Rahim Abdul Ghani, Mohd Asmadi Hussain, and Shuhaimi Mahadzir. Recent progress and future perspective of dry reforming of methane over heterogeneous catalysts. *Industrial & Engineering Chemistry Research*, 58(43):19927–19944, 2019. 10.1021/acs.iecr.9b03741.
- (20) Lihong Yu, Zhenhua Wang, Tao Wei, Fan Zhang, Huigang Xiao, and Hualin Wang. Design strategies of nickel-based catalysts for dry reforming of methane: A review. *Chemical Engineering Journal*, 460:141582, 2023. 10.1016/j.cej.2023.141582.
- (21) Nobuyuki Gokon, Zheng Wang, Haruka Yamamoto, and Tatsuya Kodama. Solar thermochemical reforming of methane with CO_2 and H_2O using Ni-ferrite/zirconia-coated foam devices. *International Journal of Hydrogen Energy*, 47(78):33326–33340, 2022. 10.1016/j.ijhydene.2022.07.251.
- (22) William H. Green. Moving from postdictive to predictive kinetics in reaction engineering. *AIChE Journal*, 66(11):e17059, 2020. <https://doi.org/10.1002/aic.17059>.
- (23) Devendra Pakhare and James Spivey. Dry reforming of methane over noble metal catalysts. *Chemical Society Reviews*, 43(22):7813–7837, 2014. 10.1039/C3CS60395D.
- (24) Mohammed Mosaad Awad, Ijaz Hussain, Umar Mustapha, Omer Ahmed Taialla, Aliyu Musa Alhassan, Esraa Kotob, AbdulHakam Shafiu Abdullahi, Saheed A. Ganiyu,

- and Khalid Alhooshani. A critical review of recent advancements in catalytic dry reforming of methane: Physicochemical properties, current challenges, and informetric insights. *International Journal of Hydrogen Energy*, 76:1–25, 2024. 10.1016/j.ijhydene.2024.03.319.
- (25) Yasotha Kathiraser, Usman Oemar, Eng Toon Saw, Ziwei Li, and Sibudjing Kawi. Kinetic and mechanistic aspects for CO_2 reforming of methane over ni-based catalysts. *Chemical Engineering Journal*, 278:62–78, 2015. 10.1016/j.cej.2014.11.143.
- (26) Juntian Niu, Yalan Wang, Shirley E. Liland, Samuel K. Regli, Jia Yang, Kumar R. Rout, Jun Luo, Magnus Rønning, Jingyu Ran, and De Chen. Unraveling enhanced activity, selectivity, and coke resistance of pt–ni bimetallic clusters in dry reforming. *ACS Catalysis*, 11(4):2398–2411, 2021. 10.1021/acscatal.0c04429.
- (27) M. Liu, A. Grinberg Dana, M. Johnson, M.J. Goldman, A. Jocher, A.M. Payne, C.A. Grambow, K. Han, N.W. Yee, E.J. Mazeau, K. Blondal, R.H. West, and C.F. Goldsmith W.H. Green. Reaction Mechanism Generator v3.0: Advances in Automatic Mechanism Generation. *Journal of Chemical Information and Modeling*, 2021. 10.1021/acs.jcim.0c01480.
- (28) Matthew S. Johnson, Xiaorui Dong, Alon Grinberg Dana, Yunsie Chung, David Farina Jr., Ryan J. Gillis, Mengjie Liu, Nathan W. Yee, Katrin Blondal, Emily Mazeau, Colin A. Grambow, A. Mark Payne, Kevin A. Spiekermann, Hao-Wei Pang, C. Franklin Goldsmith, Richard H. West, and William H. Green. Rmg database for chemical property prediction. *Journal of Chemical Information and Modeling*, 62(20):4906–4915, 2022. 10.1021/acs.jcim.2c00965.
- (29) C. Franklin Goldsmith and Richard H. West. Automatic generation of microkinetic mechanisms for heterogeneous catalysis. *The Journal of Physical Chemistry C*, 121(18):9970–9981, 2017. 10.1021/acs.jpcc.7b02133.

- (30) Connie W. Gao, Joshua W. Allen, William H. Green, and Richard H. West. Reaction Mechanism Generator: Automatic construction of chemical kinetic mechanisms. *Computer Physics Communications*, 203:212–225, 2016.
- (31) RMG developers. Reaction mechanism generator documentation, <http://reactionmechanismgenerator.github.io/rmg-py/> (accessed april 2025).
- (32) Sidney W Benson, FR Cruickshank, DM Golden, Gilbert R Haugen, HE O’neal, AS Rodgers, Robert Shaw, and R Walsh. Additivity rules for the estimation of thermochemical properties. *Chemical Reviews*, 69(3):279–324, 1969.
- (33) Katrin Blöndal, Jelena Jelić, Emily Mazeau, Felix Studt, Richard H. West, and C. Franklin Goldsmith. Computer-generated kinetics for coupled heterogeneous/homogeneous systems: A case study in catalytic combustion of methane on platinum. *Industrial & Engineering Chemistry Research*, 58(49):17682–17691, 2019. 10.1021/acs.iecr.9b01464.
- (34) Bjarne Kreitz, Patrick Lott, Jongyoon Bae, Katrín Blöndal, Sofia Angeli, Zachary W. Ulissi, Felix Studt, C. Franklin Goldsmith, and Olaf Deutschmann. Detailed microkinetics for the oxidation of exhaust gas emissions through automated mechanism generation. *ACS Catalysis*, 12(18):11137–11151, 2022. 10.1021/acscatal.2c03378.
- (35) M. P. Burke, M. Chaos, Y. Ju, F. L. Dryer, and S. J. Klippenstein. Comprehensive h_2/o_2 kinetic model for high-pressure combustion. *International Journal of Chemical Kinetics*, 44(7):444–474, July 2012. 10.1002/kin.20603.
- (36) B. Buesser. Thermodynamic library using dft and ccSD(t)-f12 with bond-additivity corrections. RMG thermochemistry library "thermo_DFT_CCSDTF12_BAC", 2022.
- (37) C.F. Goldsmith and M.R. Harper. DFT–QCI thermochemistry calculations and cantherm analysis. *J. Phys. Chem. B*, 116:9033–9042, 2012. 10.1021/jp303819e.

- (38) M.R. Harper. Additional thermochemistry from cfg in rmg’s dft_qci_thermo library. unpublished additions, 2022.
- (39) N. Quiceno and O. Deutschmann. Modeling the high-temperature catalytic partial oxidation of methane over platinum gauze: Detailed gas-phase and surface chemistries coupled with 3d flow field simulations. *Applied Catalysis A: General*, 303:166–176, 2006. 10.1016/j.apcata.2006.01.010.
- (40) D.G. Vlachos et al. A catalytic reaction mechanism for methane partial oxidation at short contact times, reforming, and combustion, and for oxygenate decomposition and oxidation on platinum. *Ind. Eng. Chem. Res.*, 46(16):5310–5324, 2007. 10.1021/ie070322c.
- (41) David G. Goodwin, Harry K. Moffat, Ingmar Schoegl, Raymond L. Speth, and Bryan W. Weber. Cantera: An object-oriented software toolkit for chemical kinetics, thermodynamics, and transport processes. Version 3.1.0, 2024. URL <https://www.cantera.org>. 10.5281/zenodo.14455267.
- (42) B. L. Gustafson and J. V. Walden. Conversion of carbon dioxide to carbon monoxide, us 5,068,057, 1991.
- (43) Jianyu Niu, Jingyu Ran, Xiaoyan Du, Wei Qi, Peng Zhang, and Lixia Yang. Theoretical analysis of the mechanism of dry reforming of methane catalyzed by a single-atom ni catalyst supported on defective graphene. *ACS Catalysis*, 11(4):2398–2408, 2021. 10.1021/acscatal.0c04429.
- (44) P. Aghalayam, Y. K. Park, N. Fernandes, V. Papavassiliou, A. B. Mhadeshwar, and D. G. Vlachos. A detailed surface reaction mechanism for methane oxidation on platinum. *Journal of Catalysis*, 213(1):23–38, 2003. 10.1016/S0021-9517(02)00044-2.
- (45) F. Zhang, M. Liu, X. Liu, Y. Su, Y. Liu, Z. Zhao, and J. Zhang. Metal-support interactions and c1 chemistry: Transforming pt-ceo2 into a highly active and stable

- catalyst for the conversion of carbon dioxide and methane. *ACS Catalysis*, 11(3):1613–1623, 2021. 10.1021/acscatal.0c04694.
- (46) Juntian Niu, Xuesen Du, Jingyu Ran, and Ruirui Wang. Dry (CO_2) reforming of methane over pt catalysts studied by dft and kinetic modeling. *Applied Surface Science*, 376:79–90, 2016.
- (47) G. Li, D.N. Zakharov, T. Hu, et al. Tracking the dynamics of catalytic pt/ceo2 active sites during water-gas-shift reaction. *Communications Materials*, 5:133, 2024. 10.1038/s43246-024-00575-4.
- (48) Pawel Mierczynski, Agnieszka Mierczynska-Vasilev, Krasimir Vasilev, et al. Fourier transform infrared spectroscopic studies of methane and liquefied natural gas reforming processes on ni/ceo2 catalyst. *Reaction Kinetics, Mechanisms and Catalysis*, 136:603–620, 2023. 10.1007/s11144-023-02362-7.
- (49) L. Liu, Q. Liu, Y. Cao, and W. P. Pan. Experimental and kinetic studies of coal-co2 gasification in isothermal and pressurized conditions. *RSC Advances*, 7:5828–5835, 2017. 10.1039/C6RA25994D.
- (50) J. Scaranto and M. Mavrikakis. Density functional theory studies of hcooh decomposition on pt(111). *Surface Science*, 648:201–211, 2016. 10.1016/j.susc.2015.11.021.
- (51) W. Gao, Q. Yang, H. Liu, and G. Li. Hcooh decomposition on pt(111): A dft study. *Surface Science*, 635:41–48, 2015. 10.1016/j.susc.2015.01.009.
- (52) L. Lin, Y. Liu, X. Zhang, and X. Ren. First-principles study of formic acid decomposition on pt(111) surface. *Journal of Molecular Catalysis A: Chemical*, 386:126–133, 2014. 10.1016/j.molcata.2014.02.016.
- (53) X. Wang, Y. Wang, S. Li, and S. Gao. Reaction mechanism insights into ch4 catalytic

- oxidation on pt13 cluster: A dft study. *Journal of Molecular Modeling*, 24(7):1–10, 2018. 10.1007/s00894-018-3729-3.
- (54) L. C. Grabow, A. A. Gokhale, S. T. Evans, J. A. Dumesic, and M. Mavrikakis. Mechanism of the water gas shift reaction on pt: First principles, experiments, and microkinetic modeling. *Journal of Physical Chemistry C*, 112:4608–4617, 2008. 10.1021/jp7099702.
- (55) P. Khandekar, C. V. Rode, R. V. Chaudhari, R. Jaganathan, and R. Seshadri. Microkinetic modeling of methane steam reforming on ni-based catalysts. *Chemical Engineering Science*, 162:75–88, 2017. 10.1016/j.ces.2016.12.040.
- (56) S. Khoobiar. Particle to particle migration of hydrogen atoms on platinum-alumina catalysts from particle to neighboring particles. *Journal of Physical Chemistry*, 68(2):411–412, 1964. 10.1021/j100784a503.
- (57) J. Im, H. Shin, H. Jang, H. Kim, and M. Choi. Maximizing the catalytic function of hydrogen spillover in platinum-encapsulated aluminosilicates with controlled nanostructures. *Nature Communications*, 5(1):3370, 2014. 10.1038/ncomms4370.
- (58) W. Karim, C. Spiel, D. Klar, S. Zafeiratos, A. M. Karim, M. Neumann, and B. Eren. Catalyst support effects on hydrogen spillover. *Nature*, 541(7635):68–71, 2017. 10.1038/nature20782.
- (59) S. Li, H. Wang, K. Hu, Y. Guo, C. Ma, T. Liu, and Y. Li. Enhanced co₂ utilization in dry reforming of methane achieved through nickel-mediated hydrogen spillover in zeolite crystals. *Nature Catalysis*, 5(7):546–554, 2022. 10.1038/s41929-022-00870-8.
- (60) Sonali Das, Ashok Jangam, Shibo Xi, Armando Borgna, Kus Hidayat, and Sibudjing Kawi. Highly dispersed ni/silica by carbonization–calcination of a chelated precursor for coke-free dry reforming of methane. *ACS Applied Energy Materials*, 3(8):7719–7735, 2020. 10.1021/acsaem.0c01122.

- (61) Hongmin Liu, Haiyang Wang, and Xingang Li. Development of efficient catalysts for CO₂ reforming of methane: Challenges and strategies. *Chemical Engineering Science*, 266:118188, 2023. 10.1016/j.ces.2023.118188.
- (62) C. Franklin Goldsmith and Richard H. West. Automatic generation of microkinetic mechanisms for heterogeneous catalysis. *The Journal of Physical Chemistry C*, 121(18):9970–9981, 2017. 10.1021/acs.jpcc.7b02979.
- (63) Knut Wittich, Michael Krämer, Nils Bottke, and Stephan A. Schunk. Catalytic dry reforming of methane: Insights from model systems. *ChemCatChem*, 12(8):2130–2147, 2020. 10.1002/cctc.201902142.